analytical chemistry

pubs.acs.org/ac Article

A Direct Z-Scheme $AgBr/CuBi_2O_4$ Photocathode for Ultrasensitive Detection of Ciprofloxacin and Ofloxacin by Controlling the Release of Luminol in Self-Powered Microfluidic Photoelectrochemical Aptasensors

Tingting Wu, Yu Du, Li Dai, Jingshuai Li, Xianzhen Song, Jinhui Feng, Xueying Wang, Qin Wei,* and Huangxian Ju*

Cite This: *Anal. Chem.* 2022, 94, 10651−10658 **Read Online**

ACCESS | Metrics & More | Article Recommendations | SI Supporting Information

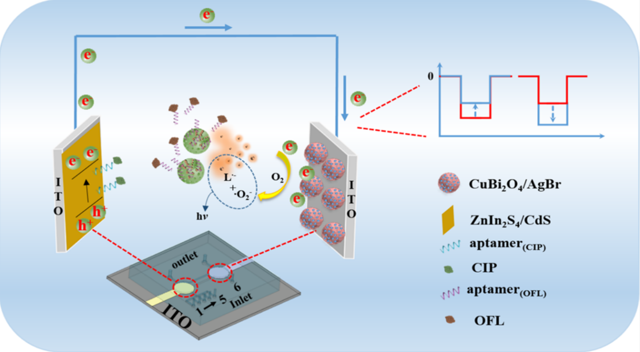

ABSTRACT: An innovative self-powered microfluidic photoelectrochemical (PEC) aptasensor was developed that uses photoactive $AgBr/CuBi_2O_4$ (ACO) composites as the photocathode matrix for ultrasensitive detection of ciprofloxacin (CIP) and ofloxacin (OFL). The formation of direct Z-scheme heterojunctions in ACO composites greatly aided electron/hole pair separation. Meanwhile, $ZnIn_2S_4$-decorated CdS nanorod arrays (CZIS) as the photoanode were used instead of a platinum counter electrode to provide electrons. The "signal-off" CIP detection was accomplished through the steric hindrance effect in the photoanode due to the combination of $aptamer_{(CIP)}$ and CIP. To increase the cathodic photocurrent intensity for OFL determination, controlled release of luminol was first used. Luminol molecules were successfully embedded in the porous structure of silicon dioxide nanospheres ($PSiO_2$) by the electrostatic adsorption between $PSiO_2$ and $aptamer_{(OFL)}$. The luminol released by specific recognition between OFL and $aptamer_{(OFL)}$ could not only react with $\bullet O_2^-$ but also produce chemiluminescence emission, resulting in the "signal-on" state. Because of the signal "on−off−on", the proposed aptasensor exhibited wide linear ranges for CIP (0.001−100 ng/mL) and OFL (0.0005−100 ng/mL) detection. Furthermore, the low detection limits of CIP (0.06 pg/mL) and OFL (0.022 pg/mL) could achieve the ultrasensitive analysis.

1. INTRODUCTION

Self-powered photoelectrochemical (PEC) sensors that can convert optical signals into electrical signals without an external voltage have attracted extensive attention.[1−3] Furthermore, the self-powered PEC sensors that integrate photoanode and photocathode, rather than redundant three-electrode systems, have a simplified structure.[1] Thus, the sensors exhibited a wide dynamic range and outstanding sensitivity in the field of biological assays,[4] pesticide residues detection,[5] and food analysis.[6] Even though the performance of the PEC sensor has reached a satisfactory level, multitarget quantitative analysis remains a challenge. Besides, one of the most pressing tasks is to develop a portable and miniaturized PEC detection platform for ultrasensitive analysis. As a result, in this paper, an analysis platform combining the benefits of a PEC sensor with a microfluidic device, such as low reagent consumption, easy integration, and compact structure,[7,8] has been proposed for ultrasensitive detection of both ciprofloxacin and ofloxacin.

Photoactive materials with superior PEC properties have recently received a lot of attention in the development of high-performance PEC sensors.[9,10] Among common semiconductor materials, n-type (e.g., TiO_2, Ag_2S) and p-type (e.g., Cu_2O, PbS) with high photocatalytic activity have been widely used as photoactive matrices or signal tags.[11,12] Nonetheless, some of the inherent drawbacks of these materials, such as low solar energy utilization and poor quantum efficiency, have gradually emerged. Consequently, it is still critical to investigate photoactive materials with exceptional photosensitivity and stability to ensure PEC performance. $CuBi_2O_4$, as a p-type semiconductor, possesses many appealing properties such as high visible light response and favorable photostability.[13]

Received: February 23, 2022
Accepted: July 11, 2022
Published: July 20, 2022

https://doi.org/10.1021/acs.analchem.2c00889

Scheme 1. (A) Construction Process of the Self-Powered Microfluidic PEC Aptasensor; (B) Preparation Process of Luminol@ $PSiO_2$-Aptamer$_{(OFL)}$ Bioconjugate

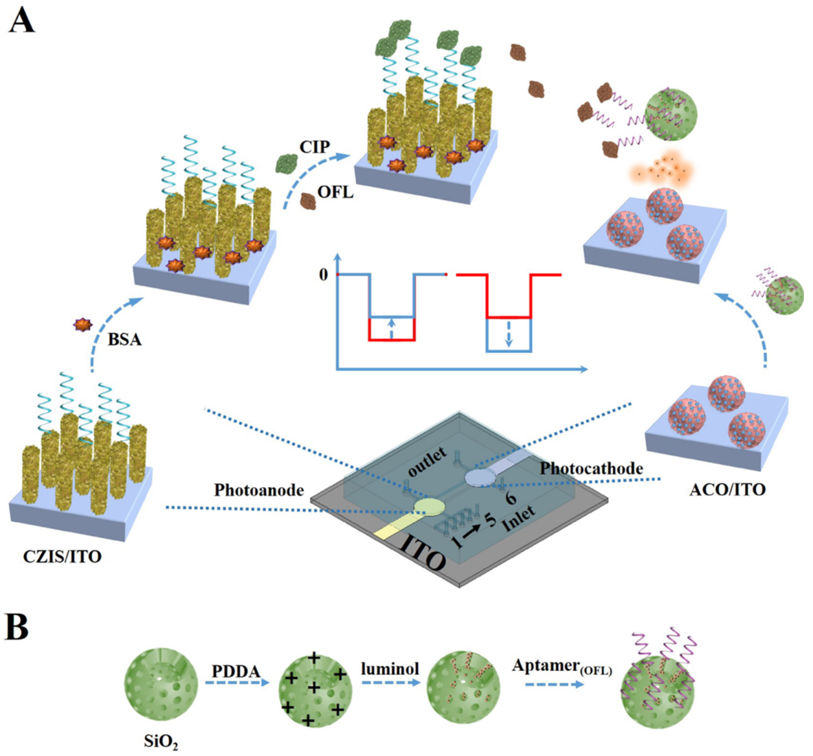

However, the high recombination of charge carrier resulted in its poor photocatalytic activity. Hence, to improve the photocatalytic properties of $CuBi_2O_4$, various semiconductor/$CuBi_2O_4$ heterojunction composites with matched band structures have been constructed, such as $CuBi_2O_4$/CuO,[14] $CuBi_2O_4$/Bi_2O_3,[15] $CuBi_2O_4$/WO_3,[16] Ag_3PO_4/$CuBi_2O_4$,[17] $CuBi_2O_4$/Bi_2MoO_6,[18] and so on. Significantly, AgBr, which possessed outstanding photosensitivity, can immensely enhance the absorption of visible light.[19,20] Based on the above, a direct Z-scheme AgBr/$CuBi_2O_4$ heterojunction composites were synthesized in this work by depositing AgBr nanoparticles onto the surface of $CuBi_2O_4$. Compared to the traditional heterojunction, the formed direct Z-scheme heterojunction between AgBr and $CuBi_2O_4$ demonstrated improved photocatalytic activity due to stronger reduction/oxidation capability and higher charge separation.[21]

Moreover, for the photocathode system, one of the key strategies for facilitating the separation of photogenerated carriers is to eliminate the superoxide anion radicals ($\bullet O_2^-$) generated by dissolved O_2. Luminol has attracted significant attention as an electrochemiluminescence (ECL) reagent due to its superior properties such as nontoxicity, water solubility, and low oxidation potential.[22] With additional investigation, the luminol-dissolved O_2 system was gradually recognized as a potential candidate in the field of ultrasensitive ECL immunoassay.[23] In Yang's previous work, for example, luminol was encapsulated in ferritin absorption as ECL labels to react with the $\bullet O_2^-$ and achieve ultrasensitive biomarkers determination.[24] In addition, Wei et al. proposed an approach that controllably released $[Fe(CN)_6]^{3-}$ as the electron acceptor to improve the photocurrent.[3] Inspired by this, a strategy of controlled release luminol to eliminate $\bullet O_2^-$ was first proposed in this paper to enhance the cathodic photocurrent of direct Z-scheme AgBr/$CuBi_2O_4$ photocathode.

In recent years, fluoroquinolone antibiotics (FAs) have been widely used in healthcare and veterinary medicine to treat bacterial infections.[6,25] FAs, in particular, exhibited extraordinary efficacy against a wide range of Gram-positive and Gram-negative pathogenic bacteria.[26,27] However, residues of FAs have emerged as potential contaminants due to their excessive production and unsafe disposal. And the presence of antibiotics in animals and surface water may badly endanger human health via the food chain.[25] Besides, FAs such as lomefloxacin, ofloxacin, enrofloxacin, norfloxacin, and ciprofloxacin may coexist in the environment making detection more difficult. Nowadays, various techniques have been applied for FA detection, such as high-performance liquid chromatography,[28] immunoassays,[29] capillary electrophoresis,[26] and enzyme-linked immunosorbent assays.[30] Nevertheless, some drawbacks including complicated pretreatment and being time-consuming and expensive limit the application of these methods. Therefore, exploring a simple, quick, and low-cost analysis technique is strongly demanded.

Herein, we designed an intriguing self-powered microfluidic PEC aptasensor using direct Z-scheme AgBr/$CuBi_2O_4$ as the photocathode matrix and $ZnIn_2S_4$ decorated CdS nanorod arrays as the photoanode to achieve multitarget quantitative analysis of both ciprofloxacin (CIP) and ofloxacin (OFL). As shown in Scheme 1, specific recognition of aptamer$_{(CIP)}$ and target in photoanode could realize a "signal-off" CIP detection. Luminol as the eliminator of $\bullet O_2^-$ was encapsulated in silicon dioxide nanospheres ($PSiO_2$) and then incubated with aptamer$_{(OFL)}$, which could amplify the cathodic photocurrent signal. The aptamer$_{(OFL)}$ specifically bound to the OFL that resulted in the aptamers$_{(OFL)}$ detaching from the surface of $PSiO_2$, meanwhile the stored luminol molecules were released,

https://doi.org/10.1021/acs.analchem.2c00889

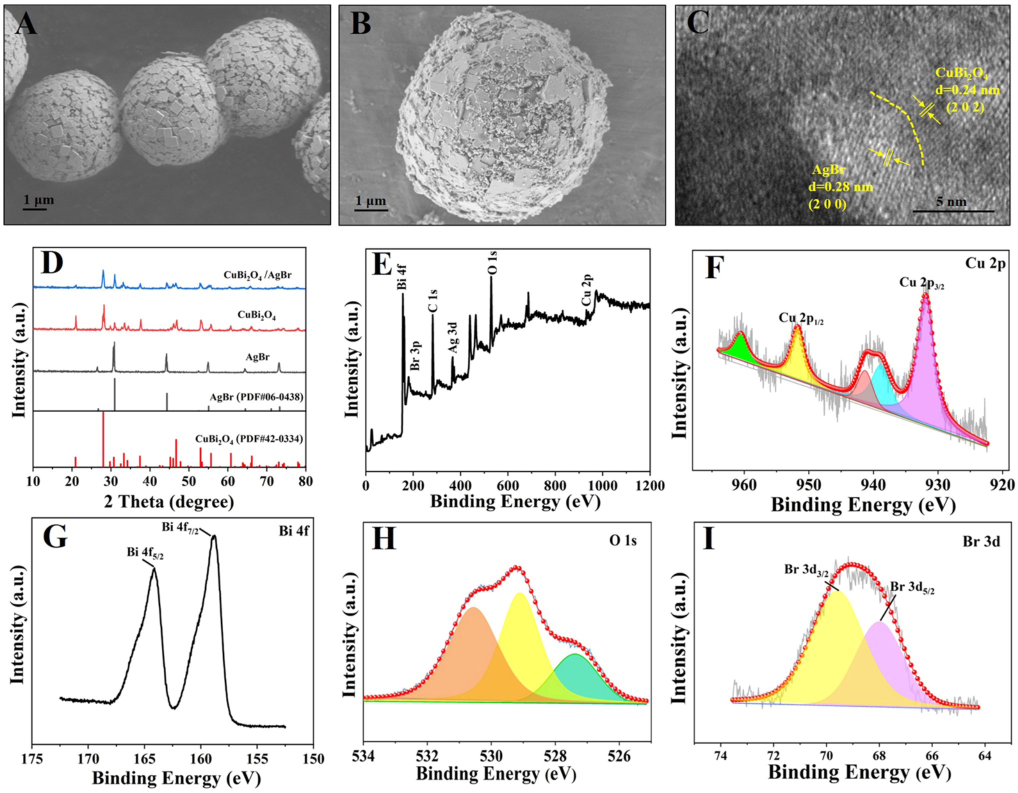

Figure 1. SEM image of (A) $CuBi_2O_4$ and (B) $AgBr/CuBi_2O_4$ composites; (C) high-resolution TEM image of $AgBr/CuBi_2O_4$ composites; (D) XRD spectrum of AgBr, $CuBi_2O_4$, and $AgBr/CuBi_2O_4$; (E) XPS pattern of $AgBr/CuBi_2O_4$; (F–I) XPS high-resolution spectrum of Cu 2p, Bi 4f, O 1s, and Br 3d.

achieving a "signal-on" response for OFL detection. Based on above, the ultrasensitive and efficient detection of CIP and OFL was carried out using the signal "on–off–on" strategy.

2. EXPERIMENTAL SECTION

2.1. Reagents and Apparatus. Materials and apparatus are given in the Supporting Information.

2.2. Preparation of Direct Z-Scheme $AgBr/CuBi_2O_4$ Composites. $CuBi_2O_4$ was synthesized using a modified hydrothermal method.[13] 1 mmol $Cu(NO_3)_2 \cdot 3H_2O$ was dissolved in 25 mL of deionized water under ultrasonic treatment for 15 min. Following that, 2 mmol $Bi(NO_3)_3 \cdot 5H_2O$ was added and stirred for 15 min. After adjusting the pH to 14, the obtained mixture was transferred into a Teflon-lined stainless-steel autoclave for 5 h at 180 °C. The prepared black products were washed and dried at 110 °C.

To prepare direct Z-scheme $AgBr/CuBi_2O_4$ composites, 20 mg of as-prepared $CuBi_2O_4$ was immersed in 20 mL of $AgNO_3$ solution (0.1 mol/L) under stirring for 3 h in dark. Then, a certain amount of KBr (0.1 mol/L) solution was added and then stirred for 3 h. Ultimately, the obtained $AgBr/CuBi_2O_4$ was collected, washed with deionized water, dried overnight, and labeled as ACO.

2.3. Preparation of Microelectrodes. Before preparation, indium tin oxide (ITO) was cut into 6 × 5 cm^2 slices. Based on the previous work, a microelectrode, which consists of a photocathode and a photoanode, was prepared by wet-etching on ITO slices (Supporting Information).[31]

2.4. Synthesis of $ZnIn_2S_4$/CdS Composites on the Photoanode. $ZnIn_2S_4$-decorated CdS nanorods arrays (CZIS) were grown on the photoanode via an improved hydrothermal reaction.[32] The details are shown in the Supporting Information.

2.5. Synthesis of the Luminol@$PSiO_2$-Aptamer$_{(OFL)}$ Bioconjugate. First, 4 mg of as-prepared $PSiO_2$ (Supporting Information) was dispersed in 4 mL of PBS. Then, 50 μL of 0.01 mol/L luminol was added and oscillated for 3 h. Then, 2 mL of aptamer$_{(OFL)}$ was added and incubated at 4 °C for 3 h. Unbounded aptamer$_{(OFL)}$ and excess luminol were removed by centrifugation and washed with PBS. Finally, the luminol@$PSiO_2$-aptamer$_{(OFL)}$ bioconjugate was dispersed in PBS containing 1% BSA and stored at 4 °C.

2.6. Manufacture Procedure of the Self-Powered Microfluidic PEC Aptasensor. On the photocathode, 15 μL of $AgBr/CuBi_2O_4$ suspension (5 mg/mL) was dropped and dried. Then microelectrodes, which included an ACO/ITO photocathode and CZIS/ITO photoanode, were then attached to polydimethylsiloxane (PDMS) microchannels (Supporting Information).

Scheme 1 depicts the construction procedure for the self-powered microfluidic PEC aptasensor. Initially, 15 μL of 3 mmol/L aqueous solution of thioglycolic acid (TGA) was injected from inlet 1. The –COOH groups were then activated by injecting 15 μL of EDC/NHS (via inlet 2). Following that, 10 μL NH_2-aptamer$_{(CIP)}$ was injected from inlet 3 and incubated at 4 °C for 1 h. Then, 8 μL of BSA (1 wt%) was incubated with the electrode (inlet 4) to avoid the nonspecific binding. After each step, the washing buffer was injected at the injection port itself to remove unabsorbed reagents.

2.7. PEC Detection of CIP and OFL. The actual object diagram and photomask designs of the microfluidic PEC aptasensor are shown in Figure S1. An LED lamp (100 W,

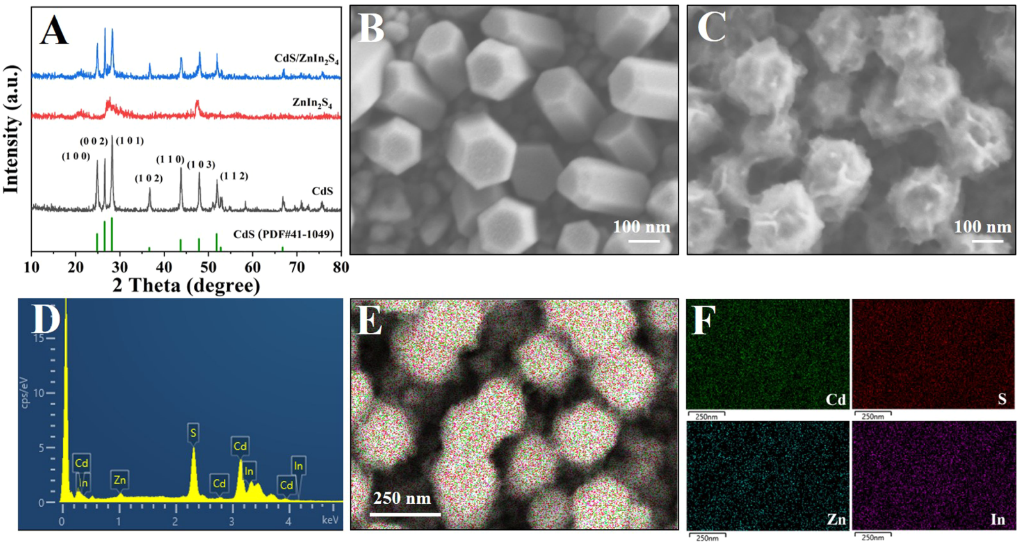

Figure 2. (A) XRD spectra of CdS, $ZnIn_2S_4$, and $ZnIn_2S_4$/CdS; SEM images of (B) CdS and (C) $ZnIn_2S_4$/CdS; (D) EDS spectrum of $ZnIn_2S_4$/CdS; (E,F) SEM elemental mapping of $ZnIn_2S_4$/CdS composites.

illumination area of 19.62 cm^2) was used as an irradiation source for PEC measurement, and tris(hydroxymethyl)-aminomethane (Tris-HCl) (pH = 8.0, 0.1 mol/L) was used as an electrolyte solution. In addition, 15 μL of the mixing solution of CIP and OFL was injected through inlet 5 and incubated for 30 min. To determine CIP, 150 μL Tris-HCl was injected to record the photocurrent response. Finally, for OFL detection, 15 μL of luminol@$PSiO_2$-aptamer$_{(OFL)}$ bioconjugate was injected from inlet 6 and incubated for 50 min and the photocurrent response was measured again.

3. RESULTS AND DISCUSSION

3.1. Characterization of the AgBr/$CuBi_2O_4$ and $ZnIn_2S_4$/CdS Composites. AgBr/$CuBi_2O_4$ composites were successfully prepared to fabricate the photocathode. The morphologies and microstructures of AgBr/$CuBi_2O_4$ composites were characterized using SEM. As seen in the SEM image in Figure 1A, the pristine $CuBi_2O_4$ sample exhibited a mean diameter of 3−4 μm with uniform nanocuboids on their surfaces. After the deposition of AgBr particles, the surface of $CuBi_2O_4$ became rough (Figure 1B). More importantly, the high-resolution TEM image in Figure 1C revealed an intimate bonding between AgBr and $CuBi_2O_4$, and the lattice fringes of 0.28 and 0.24 nm were in accord with the (2 0 0) facet of AgBr, and the (2 0 2) plane of $CuBi_2O_4$. Besides, SEM elemental mapping (Figure S3) showed a relatively uniform distribution of the five elements Cu, Bi, O, Ag, and Br, indicating that AgBr/$CuBi_2O_4$ was successfully prepared. The phase formation of the AgBr/$CuBi_2O_4$ system was investigated using an X-ray diffraction (XRD) spectrum. As depicted in Figure 1D, the XRD spectrum of $CuBi_2O_4$ showed peaks at 20.88°, 28.2°, 29.8°, 30.9°, 33.5°, 37.4°, 46.8°, 53.3°, 55.6°, and 60.7°, which could be assigned to (2 0 0), (2 1 1), (2 2 0), (0 0 2), (2 0 2) (3 1 0), (4 1 1), (4 0 2), (3 3 2), and (5 2 1), respectively. After AgBr particles were anchored, the characteristic peaks at 44.25° appeared, demonstrating that AgBr/$CuBi_2O_4$ composites were triumphantly constructed.

XPS analysis also revealed the surface chemical composition of AgBr/$CuBi_2O_4$ composites. Figure 1E shows the existence of Cu, Bi, O, Ag, and Br elements, which is consistent with EDS. As shown in Figure 1F, the peaks at 934 and 954 eV was ascribed to Cu $2p_{3/2}$ and Cu $2p_{1/2}$, respectively. Meanwhile, two shake-up satellites at around 943 and 963 eV corresponded to the $3d^9$ shell of Cu^{2+} ions.[19] Figure 1G depicts the Bi 4f spectrum, the binding energies at 158.7 and 164.1 eV were assigned to Bi $4f_{7/2}$ and Bi $4f_{5/2}$, respectively. Figure 1H presents the O 1s spectrum, the peak at 529.5 eV was attributed to lattice oxygen. Two peaks at 531.1 and 532.5 eV were ascribable to surface defects, absorbed water molecules, or chemisorbed oxygen species.[16] The Br 3d regions in Figure 1I exhibits peaks at 67.5 and 69.3 eV belonging to Br $3d_{5/2}$ and Br $3d_{3/2}$, respectively. Additionally, two peaks of Ag 3d located at 367.4 and 373.5 eV are assigned to Ag^+ in AgBr (Figure S4).

Meanwhile, as the photoanode matrix in this work, $ZnIn_2S_4$/CdS composites were successfully synthesized. Figure 2A shows the phase formation of $ZnIn_2S_4$/CdS composites; the diffraction peaks of the CdS matched well with the hexagonal wurtzite structure (JPCDS No. 41-1049). Besides, the diffraction peaks at 21.1°, 27.7°, and 47.5° were assigned to the (0 0 6), (1 0 2), and (1 1 0) planes of the hexagonal $ZnIn_2S_4$ (JCPDS No. 65-2023).[32] In the XRD spectrum of $ZnIn_2S_4$/CdS composites, both diffraction peaks of CdS and $ZnIn_2S_4$ phases are observed revealing that $ZnIn_2S_4$ has successfully grown on the surface of CdS. The SEM image in Figure 2B shows that the CdS nanostructures were hexagonal prism-like nanorods with a smooth surface and a cross-section diameter of 150−200 nm. CZIS composites were synthesized after the decoration of $ZnIn_2S_4$ (Figure 2C), it was clearly found that both the top and lateral surfaces of the CdS nanorods were covered with thin nanosheets. The EDS spectrum in Figure 2D further confirmed the elementary composition of Cd, S, and Zn in $ZnIn_2S_4$/CdS composites. Furthermore, the SEM elemental mapping in Figure 2E,F depicted the uniformly distributed elements, confirming the successful synthesis of $ZnIn_2S_4$/CdS.

Moreover, the electroactive area was an important indicator to characterize the electrochemical activity of $ZnIn_2S_4$/CdS composites. The electroactive area of $ZnIn_2S_4$/CdS nanorod arrays was measured using cyclic voltammetry. The redox peak current I_p was linearly proportional to $v^{1/2}$ (20−220 mV/s). As shown in Figure S5A,B, the regression equations of bare ITO and $ZnIn_2S_4/CdS$ modified ITO are $I = 980.06 \times \nu^{1/2}-40.78$ ($R^2 = 0.996$) and $I = 1308.89 \times \nu^{1/2} + 23.54$ ($R^2 = 0.998$), respectively. According to Randles−Sevcik equation in the Supporting Information,[24,33] the electrochemically active areas were calculated to be 0.28 and 0.38 cm^2 for bare ITO and $ZnIn_2S_4/CdS$-modified ITO. Compared with bare ITO, the electrochemically active area increased evidently, indicating the excellent electrochemical activity of $ZnIn_2S_4/CdS$ nanorod arrays.

The Fourier transform infrared spectroscopy (FTIR) was conducted to demonstrate the formation of aptamer$_{(CIP)}$-CZIS. As shown in Figure S6A, for carboxylic CZIS (curve a), the wide absorption peaks at 3450 cm^{-1} belong to the stretching vibration of O−H. The sharp absorption peak at 1700 cm^{-1} was attributed to the double-bond stretching vibration peak of C═O.[34] The peak related to C−O bending vibrations was observed at 1271 cm^{-1}. The above results confirmed the existence of carboxyl groups. After incubated with NH_2-aptamer$_{(CIP)}$ (curve b), a shoulder-type peak at 1720 cm^{-1} appeared, which indicated that the amidation reaction between CZIS and NH_2-aptamer$_{(CIP)}$ was successfully realized.[35]

3.2. Characterization of the Luminol@$PSiO_2$-Aptamer$_{(OFL)}$ Bioconjugate. Luminol@$PSiO_2$-aptamer$_{(OFL)}$ bioconjugate was synthesized for ultrasensitive detection of OFL. As the TEM image shown in Figure S6B, the prepared $PSiO_2$ exhibited a uniform spherical structure with a diameter of 150 nm. In addition, BET adsorption−desorption isotherms were conducted to prove whether luminol could encapsulate in $PSiO_2$. Figure S6C,D shows that the specific surface area of $PSiO_2$ was 644.06 m^2/g with a pore size of 2.83 nm, demonstrating excellent encapsulation ability of luminol molecules. In addition, the zeta-potentials of SiO_2, $PSiO_2$, luminol, luminol@SiO_2-aptamer$_{(OFL)}$, and luminol@$PSiO_2$-aptamer$_{(OFL)}$-OFL are shown in Figure S6E. $PSiO_2$ had a positive charge on the surface compared to SiO_2, due to the modification of PDDA. When luminol was encapsulated in $PSiO_2$ and sealed with a negatively charged aptamer$_{(OFL)}$, the zeta-potential was reversed. When OFL was added, both aptamer$_{(OFL)}$ and luminol were separated from $PSiO_2$, resulting in significantly lower zeta-potentials. UV−vis spectrum was utilized to further demonstrate the effective encapsulation of luminol inside $PSiO_2$. The supernatant was collected after centrifugation for UV−vis measurement. As shown in Figure S6F, when compared to pristine luminol solution, the characteristic peak weakened considerably after oscillated with $PSiO_2$ for 2 h. Besides, when aptamer$_{(OFL)}$ was added, the characteristic peak of luminol is further reduced. The changes of characteristic peak in the UV−vis spectrum indicated the successful encapsulation of luminol molecule.

3.3. Characterization of the Modified Electrode. For monitoring the fabrication process of the CZIS photoanode, electrochemical impedance spectroscopy (EIS) was provided in Figure 3A. The Randles equivalent circuit of Nyquist plots is exhibited in the inset and its corresponding values are presented in Table S1. The smallest semicircle of ITO indicates a low electron-transfer resistance (R_{et}) value (curve a). Then, the R_{et} value increased gradually with the decoration of CZIS (curve b), EDC/NHS (curve c), aptamer$_{(CIP)}$ (curve d), BSA (curve e), and CIP (curve f) step by step, confirming the successful construction of the CZIS photoanode.

The comparison experiments were carried out to validate the enhancement of cathodic photocurrent during OFL determination. The photocurrent of the ACO photocathode is shown in Figure 3B in the absence and presence of OFL. The photocurrent increased significantly after the addition of OFL, which could be attributed to the release of luminol from $PSiO_2$. Moreover, as illustrated in Figure S7, the photocurrent response of ACO photocathode in the microfluidic platform (curve b) has been considerably enhanced compared with the conventional detection system (curve a). This could be explained by the fact that the signal amplification effect of luminol was more obvious in microfluidic platform with smaller reaction volume. Besides, the cyclic voltammograms (CV) of ACO photocathode are shown in Figure 3C. In the absence of OFL, the luminol was encapsulated in $PSiO_2$, thus a small oxidative peak at 0.41 V was obtained.[36] In the presence of OFL, the specific combination between aptamer$_{(OFL)}$ and OFL resulting in the release of luminol. Therefore, the current peak has been significantly enhanced.

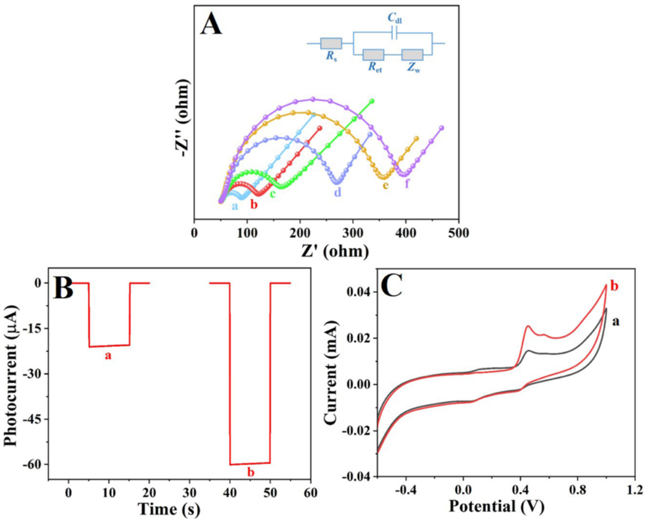

Figure 3. (A) EIS Nyquist plots and curves (a) ITO, (b) after CZIS immobilization, (c) after EDC/NHS decoration, (d) after aptamer$_{(CIP)}$ immobilization, (e) after BSA blocking, and (f) after CIP incubation. Inset in A: equivalent circuit for EIS; (B) Photocurrent response and (C) cyclic voltammograms of the ACO photocathode in the absence (a) and presence (b) of OFL.

3.4. Possible Charge Transfers Mechanism of the Proposed Microfluidic PEC Analytical Platforms. To explore the charge transfer mechanism of the as-synthesized $AgBr/CuBi_2O_4$, the linear sweep voltammetry and electronic spin resonance (ESR) experiments were carried out. As shown in Figure S8A,B, $CuBi_2O_4$ possessed a conduction band (CB) edge at −0.83 V vs Ag/AgCl (equivalent to −0.63 V vs NHE) and a valence band (VB) edge at 0.93 V vs Ag/AgCl (equivalent to 1.13 V vs NHE). Meanwhile, the CB edge and VB edge of AgBr were −0.27 V vs Ag/AgCl and 2.38 V vs Ag/AgCl, respectively, which could be converted to −0.07 V vs NHE and 2.58 V vs NHE (Figure S8C,D). Besides, the ESR experiment was applied to verify the presence of $\bullet O_2^-$. The characteristic signals of DMPO-$\bullet O_2^-$ were detected under irradiation (Figure S8E), indicating that $\bullet O_2^-$ radicals could be produced upon visible-light excited. Nevertheless, the CB of AgBr is more positive than the potential of $O_2/\bullet O_2^-$ (−0.33 eV vs NHE); thus the electrons in AgBr were unable to react with O_2 to yield $\bullet O_2^-$.[21]

Based on the forementioned analysis, the direct Z-scheme mechanism in the $AgBr/CuBi_2O_4$ was proposed. In Scheme 2, under visible light irradiation, both AgBr and $CuBi_2O_4$ can be

Scheme 2. Possible Mechanism of the Designed Sensing Platform

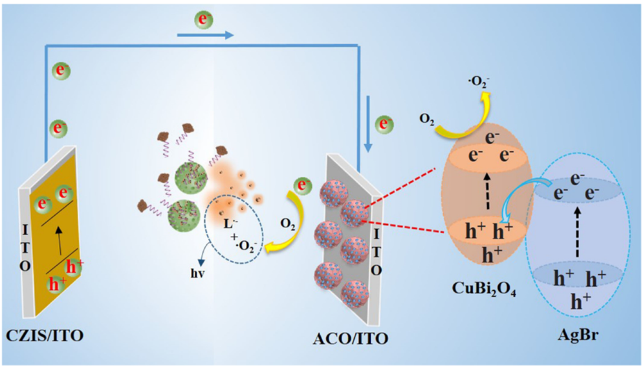

excited to generate photogenerated carriers (eq 1). The photogenerated electron on the CB of AgBr could transfer to the VB of $CuBi_2O_4$ and combined with holes. At the same time, the electrons in CB of $CuBi_2O_4$ react with O_2 to produce $\bullet O_2^-$ (eq 3). After luminol@$PSiO_2$-aptamer$_{(OFL)}$ bioconjugate was injected, luminol was released due to specific recognition between aptamer$_{(OFL)}$ and OFL. The luminol anions (luminol$^-$) generated luminol anion radicals ($L^{\bullet -}$), which could eliminate the $\bullet O_2^-$ to produce excited state 3-aminophthalate (3-AP^{2-*}) (eqs 4 and 5).[37−39] Therefore, the separation efficiency of photogenerated carriers was improved, and cathodic photocurrent intensity was enhanced. In addition, the photo-induced electrons in $ZnIn_2S_4$/CdS composites could be diverted from the photoanode to the VB of $CuBi_2O_4$ via an external circuit and react with O_2 (eq 2).

$$AgBr/CuBi_2O_4 + h\nu \rightarrow h^+ + e^- \tag{1}$$

$$ZnIn_2S_4/CdS + h\nu \rightarrow h^+ + e^- \tag{2}$$

$$O_2 + e^- \rightarrow \bullet O_2^- \tag{3}$$

$$L^{\bullet -} + \bullet O_2^- \rightarrow 3 - AP^{2-*} + N_2 \tag{4}$$

$$3 - AP^{2-*} \rightarrow 3 - AP^{2-} + h\nu \tag{5}$$

3.5. Analysis of CIP and OFL on the Self-Powered Microfluidic PEC Sensing Platform.

Under optimal experimental conditions (Figure S9), the multitarget quantitative analysis of CIP and OFL was realized based on the proposed microfluidic PEC aptasensor. The results in Figure 4A show that the photocurrent decreased as the concentration of CIP increased. As a result, a good linear relation between the change of photocurrent and logarithm of CIP concentrations (0.001−100 ng/mL) is shown in Figure 4B. The calibration plot was I (μA) = 5.63 lg $c_{(CIP)}$ − 14.4 (R^2 = 0.991) and the detection limit of CIP was 0.06 pg/mL (S/N = 3). Meanwhile, in Figure 4D, the obtained standard linear equation between PEC signal intensity and logarithm of OFL concentrations (0.0005−100 ng/mL) can be exhibited as I (μA) = −11.63 lg $c_{(OFL)}$ − 74.49, R^2 = 0.992. A low limit of OFL is attained that is 0.022 pg/mL (S/N = 3). When compared to the other methods shown in Table S2, the constructed self-powered microfluidic PEC aptasensor exhibited a wider linear range and a lower detection limit for CIP and OFL.

Additionally, stability, selectivity, and reproducibility were essential indexes to evaluate the performance of the constructed microfluidic PEC aptasensor. Extremely stable PEC signals are observed in Figure 4E, indicating the favorable stability of the proposed analytical platform. Moreover, the proposed PEC aptasensor also exhibited good storage stability (Figure S10). To investigate the selectivity of PEC aptasensor, interfering substances including enrofloxacin (ENR), tobramycin (TOB), amoxicillin (AMO), and ampicillin (AMP) were

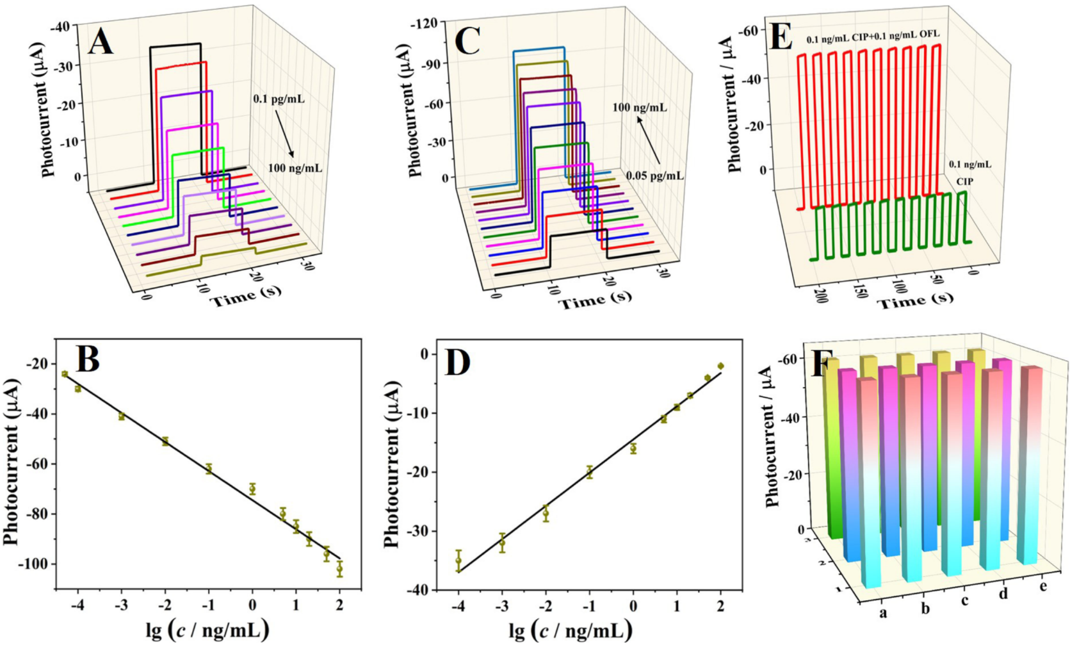

Figure 4. Photocurrent responses (A) and corresponding calibration curve (B) for CIP determination (0.1 pg/mL−100 ng/mL); photocurrent responses (C) and corresponding calibration curve (D) for OFL detection (0.05 pg/mL−100 ng/mL); (E) stability tests of the microfluidic PEC aptasensor; (F) selectivity of the analytical platforms: 0.1 ng/mL CIP + 0.1 ng/mL OFL (a), (a) +10 ng/mL ENR (b), (a) +10 ng/mL TOB (c), (a) +10 ng/mL AMO (d), and (a) +10 ng/mL AMP (e).

selected. In Figure 4F, no obvious change of photocurrent was observed, when 10 ng/mL interfering substances mixed with the mixing solution of 0.1 ng/mL CIP and OFL (three groups were implemented simultaneously), indicating satisfactory selectivity. Furthermore, the reproducibility of the PEC aptasensor for detecting 0.1, 5, and 50 ng/mL OFL was also tested. Figure S11 shows that five electrodes were constructed in the same environment to determine OFL. The results of relative standard deviation (RSD) were 2.15, 1.90, and 1.67%, respectively, indicating excellent reproducibility.

3.6. Application of the Developed Microfluidic PEC Sensing Platform in Tap Water and Milk. A standard addition method was used to verify the feasibility of the microfluidic PEC sensing platform in real samples. Briefly, 0.1 ng/mL CIP and OFL, as well as the mixture (1 ng/mL CIP + 1 ng/mL OFL) were added to tap water and milk, respectively. The pretreatments of tap water and milk are shown in the Supporting Information. Table S3 shows that the recoveries were 98.2−101.0% with RSD of 3.3−3.8% for CIP and 99.4−104.0% with RSD of 2.7−3.9% for OFL. In addition, an enzyme-linked immunosorbent assay (ELISA) kit was used as a comparison method. The F test was used to determine the precision of the designed PEC aptasensor and the ELISA kit. As shown in Tables S4 and S5, the calculated F value is lower than the 6.39 (at 95% confidence limits), which indicated no significant difference between the two methods.[40] The t test was also used to assess the accuracy of the method through comparing the mean values.[38] The t value is less than 2.78 (P = 0.95, α = 0.05, f = 4). The above results revealed that the developed microfluidic PEC sensing platform displayed potential feasibility for multitarget quantitative analysis of two types of FAs in real water and milk samples.

4. CONCLUSIONS

In a nutshell, a high-performance self-powered PEC aptasensor for ultrasensitive detection of CIP and OFL has been fabricated by integrating direct Z-scheme AgBr/$CuBi_2O_4$ photocathode with $ZnIn_2S_4$/CdS photoanode into microfluidic device. The matched band structure between AgBr and $CuBi_2O_4$ vastly promoted the charge separation and transfer. Furthermore, $ZnIn_2S_4$/CdS composites with stable photocurrent signal provided plenty of electron carriers for the PEC system. For ultrasensitive detection of CIP and OFL, luminol@$PSiO_2$-aptamer$_{(OFL)}$ was successfully synthesized to enhance cathodic photocurrent response. In the presence of OFL, aptamer$_{(OFL)}$ was detached from the surface of $PSiO_2$ and luminol released to react with $\bullet O_2^-$ and produce chemiluminescence emission. Therefore, the attenuated photocurrent caused by the steric hindrance effect during the detection of CIP was distinctly increased. Based on the signal "on−off−on," the designed microfluidic PEC aptasensor exhibited favorable stability, reproducibility, and selectivity for CIP and OFL detection. Moreover, excellent linearity for CIP (0.001−100 ng/mL) and OFL (0.0005−100 ng/mL) with a low detection limit of 0.06 and 0.022 pg/mL was achieved. More importantly, the proposed analytical platform has the potential to be a promising candidate for ultrasensitive FA analysis in environmental samples.

■ ASSOCIATED CONTENT

Supporting Information

The Supporting Information is available free of charge at https://pubs.acs.org/doi/10.1021/acs.analchem.2c00889.

Reagents, apparatus, preparation of $PSiO_2$, synthesis of $ZnIn_2S_4$/CdS composites, preparation of microelectrode, pretreatments of tap water and milk, the photomask design and actual object diagram of the microfluidic analytical platform, the wavelength range of the stimulation resource, SEM elemental mapping of AgBr/$CuBi_2O_4$ composites, XPS high-resolution spectrum of Ag 3d, cyclic voltammograms curves and linear relations of WE and $ZnIn_2S_4$/CdS modified WE, TEM image of $PSiO_2$, BET adsorption−desorption isotherms and corresponding pore size distribution of $PSiO_2$, zeta-potentials of luminol/$PSiO_2$-aptamer, UV−vis spectrums of luminol/$PSiO_2$-aptamer, cathodic and anodic linear potential scan for $CuBi_2O_4$ and AgBr, electronic spin resonance spectra of AgBr/$CuBi_2O_4$, effect of molar ratio of AgBr of the ITO/ACO electrode, influence of pH value of Tris−HCl and incubation time on the immunosensor, the storage stability of the PEC aptasensor, the reproducibility of the PEC aptasensor, simulation parameters of the equivalent circuit components, comparison of the previously reported methods for CIP and OFL detection, the results of CIP and OFL detection in tap water and milk samples by the proposed microfluidic sensing platform, analytical results of determination of CIP and OFL in tap water and milk samples (PDF)

■ AUTHOR INFORMATION

Corresponding Authors

Qin Wei − *Collaborative Innovation Center for Green Chemical Manufacturing and Accurate Detection, Key Laboratory of Interfacial Reaction & Sensing Analysis in Universities of Shandong, University of Jinan, Jinan, Shandong 250022, China;* orcid.org/0000-0002-3034-8046; Email: sdjndxwq@163.com

Huangxian Ju − *Collaborative Innovation Center for Green Chemical Manufacturing and Accurate Detection, Key Laboratory of Interfacial Reaction & Sensing Analysis in Universities of Shandong, University of Jinan, Jinan, Shandong 250022, China; State Key Laboratory of Analytical Chemistry for Life Science, Department of Chemistry, Nanjing University, Nanjing 210023, China;* orcid.org/0000-0002-6741-5302; Email: hxju@nju.edu.cn

Authors

Tingting Wu − *Collaborative Innovation Center for Green Chemical Manufacturing and Accurate Detection, Key Laboratory of Interfacial Reaction & Sensing Analysis in Universities of Shandong, University of Jinan, Jinan, Shandong 250022, China*

Yu Du − *Collaborative Innovation Center for Green Chemical Manufacturing and Accurate Detection, Key Laboratory of Interfacial Reaction & Sensing Analysis in Universities of Shandong, University of Jinan, Jinan, Shandong 250022, China;* orcid.org/0000-0002-9002-8845

Li Dai − *Collaborative Innovation Center for Green Chemical Manufacturing and Accurate Detection, Key Laboratory of Interfacial Reaction & Sensing Analysis in Universities of Shandong, University of Jinan, Jinan, Shandong 250022, China*

Jingshuai Li − *Collaborative Innovation Center for Green Chemical Manufacturing and Accurate Detection, Key*

Laboratory of Interfacial Reaction & Sensing Analysis in Universities of Shandong, University of Jinan, Jinan, Shandong 250022, China

Xianzhen Song − *Collaborative Innovation Center for Green Chemical Manufacturing and Accurate Detection, Key Laboratory of Interfacial Reaction & Sensing Analysis in Universities of Shandong, University of Jinan, Jinan, Shandong 250022, China*

Jinhui Feng − *Collaborative Innovation Center for Green Chemical Manufacturing and Accurate Detection, Key Laboratory of Interfacial Reaction & Sensing Analysis in Universities of Shandong, University of Jinan, Jinan, Shandong 250022, China*

Xueying Wang − *Collaborative Innovation Center for Green Chemical Manufacturing and Accurate Detection, Key Laboratory of Interfacial Reaction & Sensing Analysis in Universities of Shandong, University of Jinan, Jinan, Shandong 250022, China*

Complete contact information is available at:
https://pubs.acs.org/10.1021/acs.analchem.2c00889

Notes

The authors declare no competing financial interest.

■ ACKNOWLEDGMENTS

This study was supported by the National Key Scientific Instrument and Equipment Development Project of China (No. 21627809), National Natural Science Foundation of China (No. 21777056), Special Foundation for Taishan Scholar Professorship of Shandong Province, Jinan Scientific Research Leader Workshop Project (2018GXRC024, 2018GXRC021), the Innovation Team Project of Colleges and Universities in Jinan (No.2019GXRC027), the Natural Science Foundation of Shan-dong Province (ZR2020QB097).

■ REFERENCES

(1) Peng, B.; Zhang, Z.; Tang, L.; Ouyang, X.; Zhu, X.; Chen, L.; Fan, X.; Zhou, Z.; Wang, J. *Anal. Chem.* **2021**, *93*, 9129−9138.

(2) Gai, P.; Gu, C.; Hou, T.; Li, F. *Anal. Chem.* **2017**, *89*, 2163−2169.

(3) Wei, J.; Hu, Q.; Gao, Y.; Hao, N.; Qian, J.; Wang, K. *Anal. Chem.* **2021**, *93*, 6214−6222.

(4) Fan, G. C.; Lu, Y.; Zhao, H.; Liu, Q.; Li, Z.; Luo, X. *Biosen. Bioelectron.* **2019**, *137*, 52−57.

(5) Gai, P.; Zhang, S.; Yu, W.; Li, H.; Li, F. *J. Mater. Chem. B* **2018**, *6*, 6842−6847.

(6) Zhang, Z.; Liu, Q.; Zhang, M.; You, F.; Hao, N.; Ding, C.; Wang, K. *J. Hazard. Mater.* **2021**, *416*, No. 125988.

(7) Zhao, Y.; Hu, X. G.; Hu, S.; Peng, Y. *Biosens. Bioelectron.* **2020**, *166*, No. 112447.

(8) Cheng, Q.; Feng, J. H.; Wu, T. T.; Zhang, N.; Wang, X. Y.; Ma, H. M.; Sun, X.; Wei, Q. *Anal. Chem.* **2021**, *93*, 13680−13686.

(9) Yan, T.; Wu, T. T.; Wei, S. Y.; Wang, H. Q.; Sun, M.; Yan, L. G.; Wei, Q.; Ju, H. X. *Biosen. Bioelectron.* **2020**, *148*, No. 111739.

(10) Wang, Q.; Yin, H.; Zhou, Y. L.; Wang, J.; Ai, S. Y. *J. Hazar. Mater.* **2021**, *414*, No. 125293.

(11) Zhang, L. X.; Feng, L. P.; Li, P.; Chen, X.; Xu, C. C.; Zhang, S.; Zhang, A. C.; Chen, G. F.; Wang, H. *Chem. Eng. J.* **2021**, *409*, No. 128154.

(12) Dashtian, K.; Hajati, S.; Ghaedi, M. *Sens. Actuators, B* **2021**, *326*, No. 128824.

(13) Gao, Y.; Wu, J.; Wang, J.; Fan, Y.; Zhang, S.; Dai, W. *ACS Appl. Mater. Interfaces* **2020**, *12*, 11036−11044.

(14) Nogueira, A. C.; Gomes, L. E.; Ferencz, J. A.; Rodrigues, J. E.; Goncalves, R. V.; Wender, H. *J. Phys. Chem. C* **2019**, *123*, 25680−25690.

(15) Wang, Y. P.; Liu, C.; Zhang, Y. T.; Meng, W. D.; Yu, B.; Pu, S. Y.; Yuan, D. H.; Qi, F.; Xu, B. B.; Chu, W. *Appl. Catal., B* **2018**, *235*, 264−273.

(16) Wang, L. P.; Huang, T. T.; Yang, G. P.; Lu, C.; Dong, F.; Li, Y.; Guan, W. *J. Hazar. Mater.* **2020**, *381*, No. 120956.

(17) Shi, W.; Guo, F.; Yuan, S. *Appl. Catal., B* **2017**, *209*, 720−728.

(18) Shi, W. L.; Li, M. Y.; Huang, X.; Ren, H.; Guo, F.; Tang, Y.; Lu, C. *Chem. Eng. J.* **2020**, *394*, No. 125009.

(19) Wang, D.; Guo, L.; Zhen, Y.; Yue, L.; Xue, G.; Fu, F. *J. Mater. Chem. A* **2014**, *2*, 11716−11727.

(20) Hu, C.; Zhuang, J.; Zhong, L.; Zhong, Y.; Wang, D.; Zhou, H. *Appl. Surf. Sci.* **2017**, *426*, 1173−1181.

(21) Guo, F.; Shi, W.; Wang, H.; Han, M.; Guan, W.; Huang, H.; Liu, Y.; Kang, Z. *J. Hazar. Mater.* **2018**, *349*, 111−118.

(22) Wu, F. F.; Zhou, Y.; Zhang, H.; Yuan, R.; Chai, Y. Q. *Anal. Chem.* **2018**, *90*, 2263−2270.

(23) Qiao, Y. L.; Li, Y.; Fu, W.; Guo, Z. H.; Zheng, X. W. *Anal. Chem.* **2018**, *90*, 9629−9636.

(24) Yang, L.; Jia, Y.; Wu, D.; Zhang, Y.; Ju, H. X.; Du, Y.; Ma, H. M.; Wei, Q. *Anal. Chem.* **2019**, *91*, 14066−14073.

(25) Abnous, K.; Danesh, N. M.; Alibolandi, M.; Ramezani, M.; Taghdisi, S. M.; Emrani, A. S. *Sens. Actuators, B* **2017**, *240*, 100−106.

(26) Xu, X.; Liu, L.; Jia, Z.; Shu, Y. *Food Chem.* **2015**, *176*, 219−225.

(27) Drlica, K. *Curr. Opin. Microbiol.* **1999**, *2*, 504−508.

(28) He, X.; Wang, G. N.; Yang, K.; Liu, H. Z.; Wu, X. J.; Wang, J. P. *Food Chem.* **2017**, *221*, 1226−1231.

(29) Liu, X.; Xu, Z. H.; Han, Z. Y.; Fan, L. X.; Liu, S.; Yang, H.; Chen, Z.; Sun, T.; Ning, B. *Talanta* **2021**, *234*, No. 122703.

(30) Jiang, W.; Wang, Z.; Beier, R. C.; Jiang, H.; Wu, Y.; Shen, J. *Anal. Chem.* **2013**, *85*, 1995−1999.

(31) Feng, J. H.; Wu, T. T.; Cheng, Q.; Ma, H. M.; Ren, X.; Wang, X.; Lee, J. Y.; Wei, Q.; Ju, H. X. *Lab Chip* **2021**, *21*, 378−384.

(32) Zhang, G. P.; Chen, D. Y.; Li, N. J.; Xu, Q. F.; Li, H.; He, J. H.; Lu, J. M. *Appl. Catal., B* **2018**, *232*, 164−174.

(33) Wang, H.; Yuan, Y.; Zhuo, Y.; Chai, Y.; Yuan, R. *Anal. Chem.* **2016**, *88*, 2258−2265.

(34) Jia, Y.; Yang, L.; Xue, J.; Zhang, N.; Fan, D.; Ma, H.; Ren, X.; Hu, L.; Wei, Q. *ACS Sens.* **2019**, *4*, 1909−1916.

(35) Saber-Samandari, S.; Saber-Samandari, S.; Joneidi-Yekta, H.; Mohseni, M. *Chem. Eng. J.* **2017**, *308*, 1133−1144.

(36) Li, X.; Wu, D.; Ma, H.; Wang, H.; Wang, Y.; Fan, D.; Du, B.; Wei, Q.; Zhang, N. *Biosen. Bioelectron.* **2019**, *131*, 136−142.

(37) Feng, J.; Dai, L.; Ren, X.; Ma, H.; Wang, X.; Fan, D.; Wei, Q.; Wu, R. *Anal. Chem.* **2021**, *93*, 7125−7132.

(38) Li, X. J.; Du, Y.; Wang, H.; Ma, H. M.; Wu, D.; Ren, X.; Wei, Q.; Xu, J. J. *Anal. Chem.* **2020**, *92*, 12693−12699.

(39) Dong, Y. P.; Wang, J.; Peng, Y.; Zhu, J. J. *Biosen. Bioelectron.* **2017**, *94*, 530−535.

(40) Ren, X.; Ma, H.; Zhang, T.; Zhang, Y.; Yan, T.; Du, B.; Wei, Q. *ACS Appl. Mater. Interfaces* **2017**, *9*, 37637−37644.